JOURNAL OF GEOPHYSICAL RESEARCH, VOL. 115, B06312, doi:10.1029/2009JB006981, 2010

Thin and intermittent ultralow-velocity zones

Sebastian Rost,[1] Edward J. Garnero,[2] and Wolfgang Stefan[3]

Received 16 September 2009; revised 4 January 2010; accepted 13 January 2010; published 19 June 2010.

[1] An area of the core-mantle boundary to the east of Australia is investigated for the existence of ultralow-velocity zones (ULVZs). High-frequency recordings of deep Vanuatu and Tonga-Fiji earthquakes are studied from the small-aperture Warramunga Seismic Array in central Australia. The Tonga-Fiji data were used in a previous ULVZ study, while earthquakes from the Vanuatu subduction zone were newly collected for this study. Core-reflected *ScP* waves were analyzed, which possess observable precursory and postcursory arrivals in the presence of ULVZ structure. We apply a total variation deconvolution algorithm to our data, which significantly sharpens observed signals, hence, increasing our vertical resolution and therefore allowing us to detect thinner ULVZs than previously possible. The minimum ULVZ thickness detection threshold is approximately 2–3 km with this method. This data set samples a spot at the boundary of the large low shear velocity province beneath the Pacific. The new analysis provides evidence for a 5–6 km thick ULVZ to the north of a previously detected 8.5 km thick ULVZ. A second sampled region shows evidence for an even thinner ULVZ structure, with thicknesses of ~3 km. These findings are largely consistent with the hypothesis that ULVZs are most likely to be found along the inside margin of large low shear velocity regions that have been attributed to dense, chemically distinct material.

Citation: Rost, S., E. J. Garnero, and W. Stefan (2010), Thin and intermittent ultralow-velocity zones, *J. Geophys. Res.*, *115*, B06312, doi:10.1029/2009JB006981.

1. Introduction

[2] The last 20 years have witnessed a tremendous increase in our knowledge and understanding of the processes at the contact zone between the molten iron of the core and the silicate mantle at the core-mantle boundary (CMB). The structures detected at this contact zone indicate that this boundary is far from being a simple first-order discontinuity separating iron and silicate [*Bullen*, 1949; *Dziewonski and Anderson*, 1981]. Although there are many aspects of the chemistry, rheology, and dynamics of this deep region of the Earth that are still not understood, there is consensus that the CMB as a chemical and thermal boundary layer is crucially important for our understanding of how our planet works [*Nakagawa and Tackley*, 2004; *Tolstikhin and Hofmann*, 2005; *van der Hilst et al.*, 2007; *Garnero and McNamara*, 2008].

[3] The lowermost mantle just above the CMB, i.e., the D″ region, shows evidence for multiscale heterogeneities and layering, as well as anisotropy. Recent findings include (1) an intermittent discontinuity some 200–300 km above the CMB, called the D″ discontinuity, with strong topography [*Lay and Helmberger*, 1983; *Thomas et al.*, 2004; *Kito et al.*, 2007; *van der Hilst et al.*, 2007; *Hutko et al.*, 2008], (2) strong anisotropy over the lowermost few hundred kilometers [*Kendall and Silver*, 1996; *Lay et al.*, 1998; *Garnero et al.*, 2004; *Rokosky et al.*, 2006; *Wookey and Kendall*, 2008], (3) increased small-scale heterogeneities compared to mid-mantle depths [*Cormier*, 1999; *Garnero*, 2000], (4) scattering from small-scale heterogeneities [*Bataille and Lund*, 1996; *Earle and Shearer*, 1998; *Vidale and Hedlin*, 1998; *Hedlin and Shearer*, 2000; *Thomas et al.*, 2009], (5) thin layers of strongly reduced velocity right at the CMB on the mantle side, called ultralow-velocity zones (ULVZs) [*Garnero and Helmberger*, 1995; *Mori and Helmberger*, 1995; *Wen and Helmberger*, 1998; *Rost and Revenaugh*, 2003; *Rost et al.*, 2005, 2006; *Idehara et al.*, 2007], and (6) indications of layered structure in the outermost few kilometers of the core related to CMB processes [*Buffett et al.*, 2000; *Rost and Revenaugh*, 2001; *Helffrich and Kaneshima*, 2004].

[4] ULVZs are characterized by strong decreases in *P* wave and *S* wave velocities in the range of 10%–30% relative to 1-D Earth models [*Garnero and Helmberger*, 1995]. Recent studies indicate that ULVZ material shows higher density than the surrounding mantle [*Rost et al.*, 2005, 2006; *Garnero et al.*, 2007; *Idehara et al.*, 2007]. Significant trade-offs are present in modeling ULVZ with most probes, particularly between ULVZ thickness and magnitude of velocity reduction [*Garnero and Helmberger*, 1998]. Some studies have noted thin low-velocity layering at the CMB

[1]Institute of Geophysics and Tectonics, School of Earth and Environment, University of Leeds, Leeds, UK.
[2]School of Earth and Space Exploration, Arizona State University, Tempe, Arizona, USA.
[3]Department of Computational and Applied Mathematics, Rice University, Houston, Texas, USA.

0148-0227/10/2009JB006981

but not necessarily ultralow reductions (e.g., < 10%) [*Avants et al.*, 2006a, 2006b; *Lay et al.*, 2006].

[5] Several mechanisms have been proposed to explain the strong ULVZ velocity reductions. Partial melting of some component of the deep mantle is most commonly invoked as the origin of the ULVZ [*Williams and Garnero*, 1996; *Revenaugh and Meyer*, 1997; *Vidale and Hedlin*, 1998; *Wen and Helmberger*, 1998; *Wen*, 2000; *Lay et al.*, 2004; *Rost et al.*, 2005, 2006; *Labrosse et al.*, 2007] as a means of explaining the approximately 1:3 ratio of *P* wave to *S* wave velocity reductions found in some studies [*Williams and Garnero*, 1996; *Berryman*, 2000]. Other explanations for the ULVZ include accumulated silicate sediments from the core [*Buffett et al.*, 2000; *Rost and Revenaugh*, 2001], subducted rocks containing banded iron formations [*Dobson and Brodholt*, 2005], and iron-enriched postperovskite [*Mao et al.*, 2006]. For some structures, the notion of a blurred CMB interface has been discussed [*Garnero and Jeanloz*, 2000]. We also note the possibility that more than one of these mechanisms may simultaneously (separate or combined) act to create ULVZs on Earth.

[6] Because of source-receiver restrictions and few seismic probes being sensitive to ULVZ structure, only a part of the CMB area has been studied for ULVZ existence [*Thorne and Garnero*, 2004; *Garnero et al.*, 2007]. The greatest coverage of the globe, roughly 45% of the CMB's surface area, has been obtained using core phases with short segments of *P* wave diffraction, called SP_dKS [*Garnero and Helmberger*, 1995; *Garnero et al.*, 1998; *Wen and Helmberger*, 1998; *Rondenay and Fischer*, 2003; *Thorne and Garnero*, 2004]. While many regions show strong evidence for ULVZ structure, many of these studies indicate there are regions that lack a ULVZ, or alternatively, that ULVZ layering is below the detection threshold level of SP_dKS (e.g., either too thin or too weak). The SP_dKS phase is strongly sensitive to elastic properties right at the CMB since it owes its existence to the critical angle in a *S*-to-*P* conversion at the CMB. Larger distance SP_dKS waves have longer P_{diff} segments and, hence, provide information about the integrated path along the CMB.

[7] While SP_dKS waves are the most sensitive to ULVZ properties right at the CMB, the elastic properties of the top of the ULVZ (i.e., its contrast with the overlying mantle) are best illuminated with short-period topside reflected waves. This modeling focuses on identifying and modeling precursors to core-reflected phases *PcP*, *ScP,* and *ScS* [*Vidale and Benz*, 1993; *Mori and Helmberger*, 1995; *Revenaugh and Meyer*, 1997; *Castle and van der Hilst*, 2000; *Rost and Revenaugh*, 2003; *Idehara et al.*, 2007; *Avants et al.*, 2006a]. In addition to better vertical resolution, the core reflection data have improved lateral resolution than SP_dKS. These data also show regions having [*Rost et al.*, 2005, 2006; *Idehara et al.*, 2007] and lacking [*Vidale and Benz*, 1992; *Castle and van der Hilst*, 2000; *Reasoner and Revenaugh*, 2000; *Persh et al.*, 2001; *Rost et al.*, 2010] ULVZ structure. Taken together, the core-reflected and diffracted data support the notion that ULVZs are a regional phenomenon at the base of the mantle and are not ubiquitous.

[8] Understanding the geographical distribution of ULVZs may figure prominently in mapping deep mantle flow and chemistry [*Garnero and McNamara*, 2008]. One challenge, however, is that seismic ULVZ nondetections do not rule out the possibility of thin or weak ULVZ layering that may go undetected. The threshold of thickness for ULVZ detectability depends on the seismic probe, the ULVZ velocity and density, and the dominant frequency of the data employed.

[9] The following presents a study of *ScP* waveforms of two neighboring regions of the CMB east of Australia that are sampled by data from a central Australian short-period seismic array. Using a deconvolution method based on total variation [*Stefan et al.*, 2006], we improve our ability to detect *ScP* waveform variations and therefore to detect thin ULVZs and to find evidence for ULVZs that were previously below the limit of seismic detection. We report evidence for an ultrathin ULVZ that surrounds an area previously mapped with a thicker ULVZ [*Rost and Revenaugh*, 2003; *Thorne and Garnero*, 2004; *Rost et al.*, 2005; *Garnero et al.*, 2007].

2. Short-Period Array Data

[10] We use recordings from the permanent Australian Warramunga SeismicArray (WRA). WRA consists of 20 short-period vertical seismometers deployed along two 20 km long branches, forming an L-shaped array. The interstation spacing is ~2.25 km, optimizing WRA for the detection of 1 Hz *P* waves [*Cleary et al.*, 1968]. We use WRA recordings from sources in the Tonga-Fiji and Vanuatu subduction zones (Figure 1). The data from Tonga-Fiji dominantly sample the CMB near longitude 168° and latitude −22° to −26° (hereafter referred to as "region 1"), which was previously investigated for ULVZ structure by *Rost et al.* [2005]. Their study found evidence for a small-scale (~50 km wide) ULVZ with an average thickness of 8.5 km, *P* wave and *S* wave reductions of −8% and −25%, respectively (relative to preliminary reference Earth model (PREM)), and a 10% density increase. Further evidence for ULVZ structure in this region comes from data of the Alice Springs Array (ASAR) [*Rost et al.*, 2006]. We revisit the WRA data set using a new deconvolution method and compare the results from region 1 to data from the neighboring Vanuatu source region.

[11] Data from Vanuatu sample to the west of region 1 roughly near longitude 158° and latitude between −15° and −23° (hereafter referred to as "region 2"), which has not been analyzed for ULVZ structure before. The earthquakes collected to investigate this region occurred between 1990 and 1998; their magnitudes range from 4.2 to 5.7, and source depths range between approximately 100 and 700 km. Source-receiver distances range between approximately 41° and 47° for region 1 and between approximately 31° and 36° for region 2. In total, the data set consists of ~1000 earthquakes (~475 from the Tonga-Fiji region sampling region 1 and ~500 newly collected earthquakes from the Vanuatu region sampling region 2).

[12] The distance range for these data has been shown to be well suited for robust and clear *ScP* observations. Thus, we analyze seismic array data in the time immediately preceding and following *ScP* arrivals for the presence of precursors and postcursors, respectively, which result from ULVZ structure [*Garnero and Vidale*, 1999; *Reasoner and Revenaugh*, 2000; *Rost and Revenaugh*, 2003; *Rost et al.*,

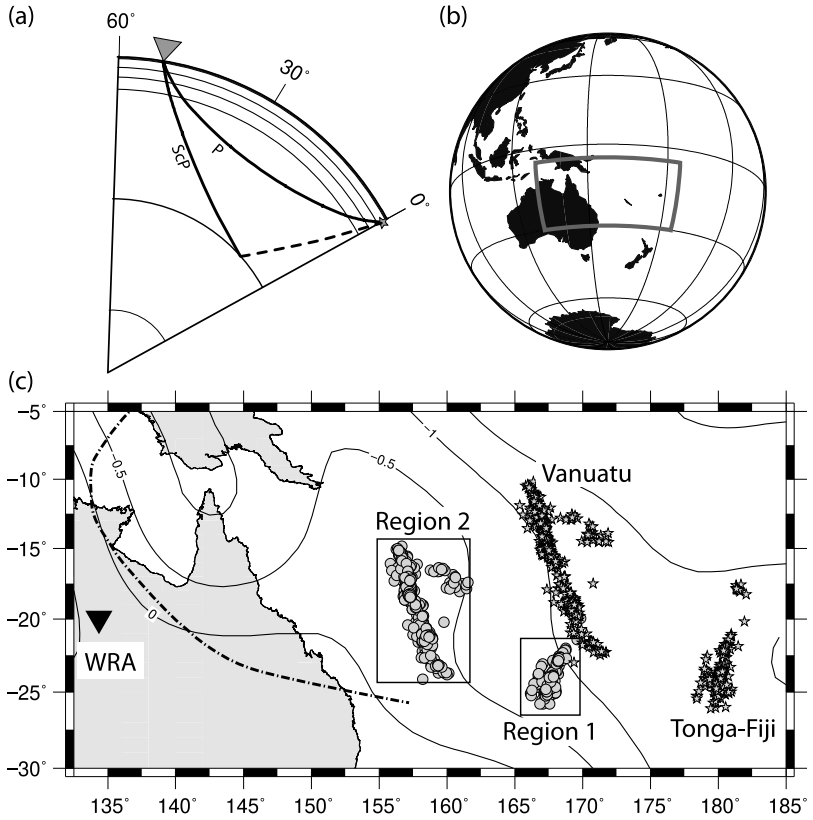

Figure 1. (a) Ray configuration used in this study. *ScP* starts as a *S* wave (dashed) at the source location and converts to a *P* wave upon reflection at the CMB. (b) Study area outline. (c) Details of the study area showing earthquakes (stars) and location of WRA (triangle). The *ScP* CMB reflection points are indicated by circles. Contours indicate the velocity reductions relative to a reference model from *Ritsema and van Heijst* [2002]. Dot-dashed line indicates the possible edge of the LLSVP in this region as determined by *He et al.* [2006]. The location of the LLSVP beneath eastern Australia is only weakly constrained in this study but seems to follow the 0% *S* wave velocity contour of the tomography model.

2006; *Idehara et al.*, 2007]. The source locations and *ScP* CMB conversion points for the complete data set are shown in Figure 1c.

[13] From the original data set we select events that show *ScP* arrivals in raw individual traces upon visual inspection for further analysis using a new deconvolution approach. This reduces the data set to 301 events sampling region 1 and 74 events sampling region 2. This is the data set used for the t^* analysis discussed in section 3.2. The difference in quantity of high-quality *ScP* arrivals between these two source regions primarily stems from the larger number of deep earthquakes in the Tonga-Fiji region. Deep earthquakes, in general, show larger *ScP* amplitudes since the *ScP* paths originate below the highly attenuating upper mantle. For these selected events, array beam traces [*Rost and Thomas*, 2002] are formed using the *ScP* slowness and back azimuth measured by the frequency-wave number analysis method [*Capon*, 1969; *Rost and Thomas*, 2002]. The array beam forming improves the signal-to-noise ratio (SNR) of a coherent signal by summing the individual recordings of the array stations taking into account the time offsets due to the lateral distribution of the seismic stations and the incident angle of the seismic wavefront [*Rost and Thomas*, 2002].

[14] We will employ the total variation (TV) deconvolution method [*Stefan et al.*, 2006] to sharpen the *ScP* arrivals to improve our ability to detect possible precursors and postcursors to *ScP*. The TV deconvolution is very sensitive to the SNR of the data since this method redefines the whole trace as new time series of sharp, boxcar-like signals, which, when convolved with a point spread function (PSF), reproduce the observed seismogram [*Stefan et al.*, 2006]; this method works best with high signal-to-noise signals. To select the best SNR data, we calculate an *ScP* SNR defined by the maximum peak amplitude measured in a 10 s signal time window centered on *ScP* compared to the peak amplitude measured in a time window presumed to represent the background noise level from −20 to −5 s before the *ScP* onset. We retain recordings with an SNR larger than 7; example beam waveforms sampling regions 1 and 2 are shown in Figures 2a and 2b, respectively. Our data set that fulfills this criterion reduces to 90 events sampling region 1 and 19 events sampling region 2. The *ScP* beam waveforms of this final data set are shown in a back azimuth-dependent display which results in roughly north-south oriented pro-

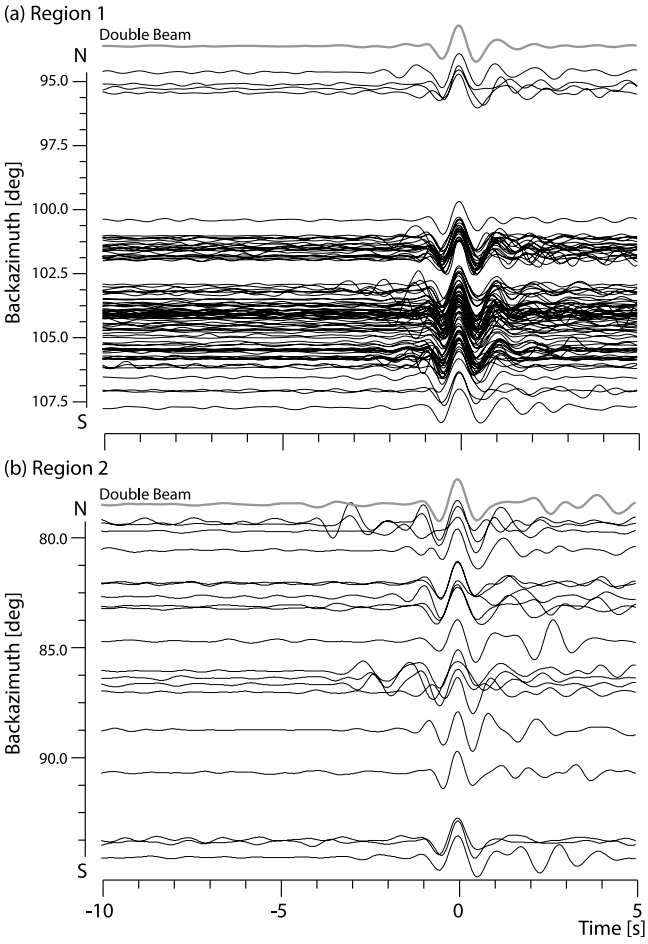

Figure 2. Back azimuth sorted *ScP* beam traces selected from the data set (*ScP* SNR larger than 7). Traces are aligned on *ScP* and normalized to the maximum amplitude in each trace. Traces are sorted with respect to their back azimuth measured at WRA. This allows a roughly north-south oriented data profile along the CMB in both regions because of location of the seismicity almost due west of WRA. (a) Ninety traces sampling region 1. (b) Nineteen traces sampling region 2.

files along the CMB due to the location of the seismicity due east of WRA. The event parameters for the final data set are given in the auxiliary material.[1]

[15] Although some *ScP* precursory energy can be detected in this data set, these precursors are generally incoherent over a larger back azimuth range, i.e., over several neighboring traces. This could indicate that ULVZs exist on short lateral scales in both regions, e.g., in small individual patches of ULVZ structure perhaps only a few kilometers wide influencing a single *ScP* reflection point. Between these patches the ULVZ structure could either be absent or too weak and/or too thin to produce *ScP* waveform variations that can be detected in the high-quality array recordings even after array beam forming. The following analysis tries to test this hypothesis by using a deconvolution method to sharpen the *ScP* waveforms which might allow the identification of precursors and postcursors close to *ScP* that are not visible in the original waveforms because of waveform interference.

3. Analysis

[16] Standard slant stacking of *ScP* waveforms suggests the absence of large-scale coherent ULVZ structure in both study regions because of the lack of *ScP* precursors being identified over a larger back azimuth range. However, the threshold for ULVZ detection (i.e., the thickness of the thinnest detectable ULVZ) is strongly dependent on the dominant period of *ScP* since ULVZ detections are most robust if *ScP* precursors are independently identifiable in front of *ScP*. In other words, it is difficult to identify *ScP* precursors that arrive within a wavelength of *ScP*. In this section we explore an approach to "sharpen" the *ScP* phase through deconvolution, which allows us to identify *ScP* precursors and postcursors with very short differential traveltimes to *ScP*, which permits the detection of thinner ULVZs than previously possible.

3.1. Broadened *ScP* Observations

[17] *Rost et al.* [2005] documented strong broadening of the *ScP* waveforms (relative to the direct *P* wave) from deep focus Tonga-Fiji earthquakes to WRA and explored increased lower mantle attenuation as a mechanism to explain the data. This is the same path as for region 1 in this study. Alternatively, *Rost et al.* [2005] discussed the possibility that a very thin ULVZ (e.g., <5 km thick) would produce *ScP* precursors and postcursors, but because of the finite frequency of the WRA data and the small differential traveltimes between the additional phases and *ScP*, the extra arrivals would not be distinguishably separated from *ScP*. Thus, constructive waveform interference would lead to the appearance of broadened *ScP* pulses.

3.2. Assessing Deep Mantle Attenuation

[18] Since *ScP* traverses the deep mantle independently from *P*, the *ScP* broadening we observe can be due to deep mantle attenuation. We study differential attenuation between *P* and *ScP* by finding the best fit t^* parameter that best maps the *P* wavelet into the broadened *ScP* wavelet. The t^* operator describes the attenuation of body waves and is the ratio of the body wave traveltime to the quality factor Q integrated along the raypath [*Carpenter and Flinn*, 1965; *Bock and Clements*, 1982]. We find that a lowermost mantle lacking strong attenuation, like the 1-D Earth model PREM, results in a *ScP*-to-*P* differential attenuation t^* of ~0.15 s [*Rost et al.*, 2005]. *ScP* waveforms for this study range from $t^* = 0.15$ to t^* values larger than 0.6 s. Figure 3 displays examples of *P* and *ScP* waveforms along with the *P* wave convolved with the t^* operator that best maps the *P* wave into *ScP*. For smaller t^* values in the range of 0.1 s, the *P* and *ScP* waveforms are very comparable (Figure 3a), while waveforms best fit with slightly larger values of $t^* = 0.4$ s already show a pronounced broadening of the *ScP* waveform compared to *P* (Figure 3b). The largest values of t^*, which are in the range of $t^* = 0.8$ s (Figure 3c), correspond to a stronger waveform broadening of *ScP* relative to *P*.

[1] Auxiliary materials are available in the HTML. doi:10.1029/2009JB006981.

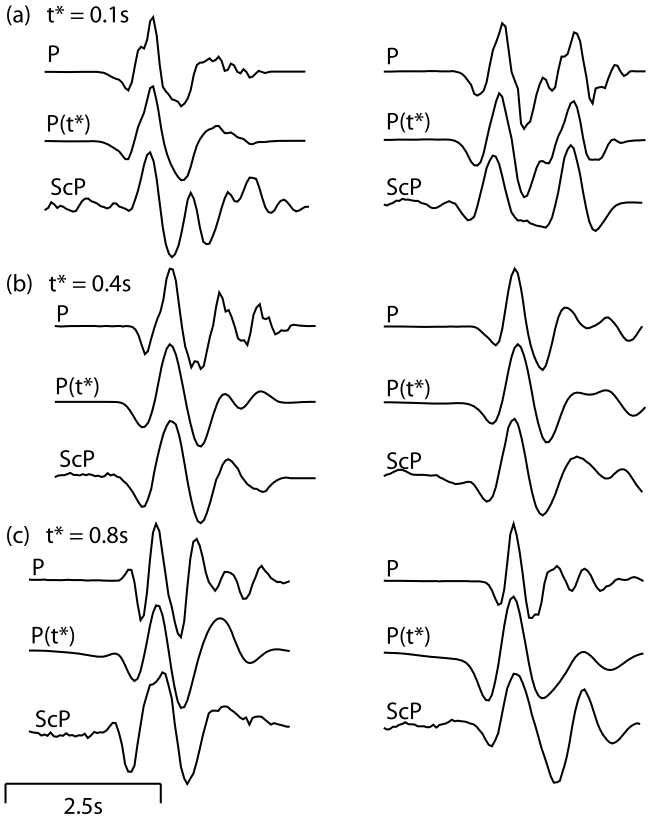

Figure 3. Examples of *ScP* waveforms that are best predicted by large and small t^* operators applied to the *P* wavelet of the same event. (a) Examples of a *ScP* waveforms best fit with a $t^* = 0.1$ s applied to the initial *P* wavelet for events on (left) 9 September 1996, 0932:00 UT, and (right) 16 August 1995, 0122:00 UT. Top trace shows the *P* wavelet for comparison, the middle trace shows the *P* waveform after application of the t^* operator, and the bottom trace shows the recorded *ScP* waveform. (b) Same as Figure 3a except for a t^* of 0.4 s for events on (left) 4 April 1994, 0012:00 UT, and (right) 12 July 1991, 1459:00 UT. (c) Same as Figure 3a except for a large t^* value of 0.8 s for events on (left) 6 October 1991, 0723:00 UT, and (right) 30 December 1991, 0008:00 UT.

[19] We are able to obtain 213 stable t^* measurements for region 1 and 65 for region 2 using the initial data set of detectable *ScP* arrivals in raw waveforms (in total 301 events sampling region 1 and 74 events sampling region 2). The geographical distribution of t^* values mapped to *ScP* reflection points is shown in Figure 4. The results for region 1 are similar to the ones reported by *Rost et al.* [2005]. The most anomalous t^* values ($t^* > 0.6$ s) predominantly cluster in region 1 mainly to the north of where *Rost et al.* [2005] identified a 8.5 km thick ULVZ structure, although some broadened waveforms might also originate from this ULVZ region (as indicated by the gray ellipse in Figure 4). Their study and this study both find abundant *ScP* data that sample the *Rost et al.* [2005] ULVZ that do not require anomalous t^* values. This can be understood since a thicker ULVZ will create larger differential traveltimes between the precursors and postcursors and *ScP*, allowing a clear separation of the precursors and postcursors and *ScP*. The main *ScP* arrival will therefore not be influenced by the waveform interference of the precursors and postcursors and will be best fit by a *P* wavelet convolved with a small t^* value.

[20] If ULVZs owe their existence to partial melt of some deep mantle constituent, it is reasonable to expect the strongest *ScP* attenuation to occur for data that traverse the ULVZ. But since many data that sample the ULVZ are not broadened and many data that are very broadened are associated with CMB regions appearing to lack thick ULVZ, we are motivated to consider another mechanism for the most anomalous *ScP* broadening that we observe.

3.3. Total Variation Deconvolution

[21] Here we explore the possibility that broadened *ScP* waveforms are caused by waveform interference between the main *ScP* arrival and precursors and postcursors originating from a thin ULVZ (i.e., less than ~6 km thick). The strong lateral changes of t^* observed here are difficult to explain with very small scale attenuation structure. Therefore, the interference of *ScP* with phases generated by the interaction of *ScP* with ULVZs might provide a simple explanation for the observed waveforms. To increase the sensitivity of *ScP* as a probe for very thin ULVZs, we use TV deconvolution, a blind deconvolution method that sharpens the arrival onset using an empirical source deconvolution [*Stefan et al.*, 2006]. For each event, we use the array beam of the direct *P* wave arrival recorded at WRA as a proxy for the source time function, which defines the point spread function used in this deconvolution method. We use a trade-off parameter between the smoothness of the reconstruction and the fit of the data of 1.0 [*Vogel*, 2002; *Stefan et al.*, 2006]. Experiments with different values of this parameter show that this provides a good fit to the data provided the noise conditions around *ScP*. Details of the TV deconvolution method applied to seismic data are given by *Stefan et al.* [2006].

[22] Examples of deconvolved *ScP* and *P* waveforms using the TV deconvolution are shown in Figures 5a and 5b, where it is applied to synthetic data. We demonstrate the method with elastic Gaussian beam synthetics [*Cerveny*, 1985; *Weber*, 1988] through a 1-D Earth model including ULVZs of different thicknesses. The velocity structure above the ULVZ is identical to PREM, the ULVZ velocity reductions are 10 % and 30%, for *P* and *S* waves, respectively, and the ULVZ contains a 10% density increase. We use the application Xgbm by *Davis and Henson* [1993] to calculate the synthetic seismograms. We use a line source as source mechanism with a short 0.6 s Gaussian wavelet width to produce an approximate spike train for a simplified seismogram containing the *P* and *ScP* arrivals as well as *ScP* precursors (*SdP* and *SPcP*) and postcursors (*ScSP*) similar to that used by *Rost and Revenaugh* [2003]. This spike train contains the amplitude and timing information from the path through the 1-D Earth model and the interaction of *ScP* with the ULVZ. We then convolve this trace with a *P* wavelet from the recorded data set as a representative of a finite source time function from the data set and the instrument response of the WRA recording system to obtain a synthetic *ScP* waveform that can be compared to the recorded data.

[23] Using the same source time function from the *P* wavelet as PSF in the TV deconvolution leads to a boxcar shape of the *P* arrival after the deconvolution, sharpening

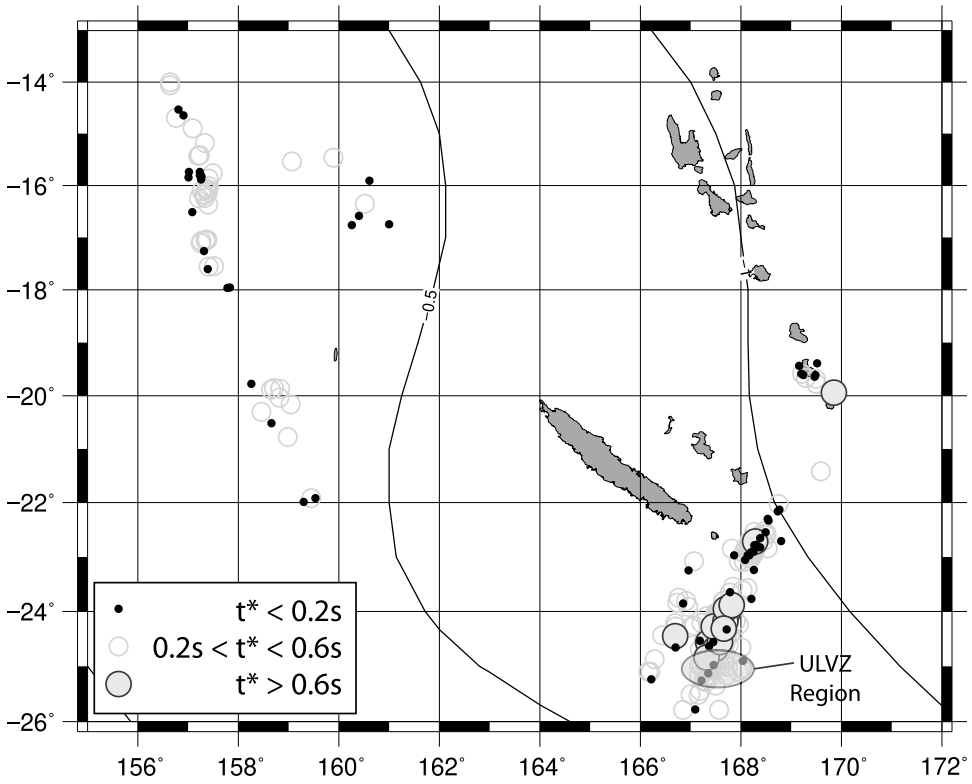

Figure 4. Map of t^* values found to best fit the *ScP* broadening observation. Black dots indicate *ScP* waveforms that are best fit by $t^* < 0.1$ s applied to the *P* wavelet. Open circles indicate 0.2 s < t^* < 0.6 s, and large shaded circles indicate large t^* values larger than 0.6 s. These large values are mainly found in region 1 to the north of a ULVZ region found by *Rost et al.* [2005] as indicated by the gray ellipse. Most *ScP* waveforms in region 2 are best fit by medium t^* values of 0.2 s to 0.6 s. Contour lines indicate velocity changes as found by tomography [*Ritsema and van Heijst*, 2002].

the arrival tremendously (e.g., top trace of Figure 5a). For a ULVZ of 10 km thickness (Figure 5a) the deconvolved *ScP* waveform clearly shows the individual arrivals that are generated by the interaction of the *ScP* wavefield with the ULVZ structure. The process clearly predicts the three additional phases that were modeled using Xgbm. This example shows that the TV deconvolution is able to extract better timing information from the synthetic data and can lead to a higher accuracy of measuring differential traveltimes. The improvement of resolution of thinner ULVZs through TV deconvolution is shown in Figure 5b. The ULVZ in this model is only 2 km thick with velocity and density variations as for the 10 km thick model (shown in Figure 5a). Such a thin ULVZ is well below the resolution level of even high-frequency array methods [*Rost et al.*, 2006]. The *ScP* deconvolved trace clearly shows a small but distinctive precursor to the main arrival *ScP*. No such additional arrival can be identified in the deconvolved *P* wavelet; that is, the additional energy is unique to the *ScP* path and is due to interaction with the ULVZ.

[24] The SNR of *P* and *ScP* in observations is obviously lower than in synthetic calculations, but tests show that the TV deconvolution method is stable for high SNR WRA data as selected with the high SNR cutoff here. Examples of the deconvolution of *ScP* sampling regions 1 and 2 are shown in Figures 5c–5h. The deconvolution simplifies the *P* wavelet strongly, normally leading to a simple narrow boxcar shape marking the first arrival and few, if any, coda arrivals. In most cases the deconvolved *ScP* waveforms show a simple boxcar shape similar to the deconvolved *P* waveform (Figures 5c and 5d), indicating no *ScP* waveform variation compared to *P*. This indicates that no ULVZ structure, or ULVZ structure even below the deconvolution resolution level, is present at the *ScP* reflection point. Nonetheless, several events show clear precursors in the deconvolved *ScP* waveforms (Figures 5e–5h). The differential time between the precursor and *ScP* varies from ~0.5 to ~1.3 s. This translates to ULVZ thicknesses from 2–3 km to 5–6 km assuming 10% V_P and 30% V_S velocity reductions. The 8.5 km thick ULVZ detected by *Rost et al.* [2005] would produce a ~2 s precursor to *ScP*. We conclude that the TV deconvolution greatly improves the vertical resolution capability of *ScP* to detect thin ULVZs down to about 2–3 km; the detection of thin ULVZs with high-quality deconvolved data is therefore possible.

4. Discussion

[25] Our analysis finds evidence for *ScP* precursors arriving less than 2 s before *ScP* that suggests the existence of very thin ULVZ structure in the two regions studied. Figure 6 shows a map of the precursor detections from the TV deconvolved *ScP* waveforms. We categorize the precursor detections into three groups: (1) no *ScP* waveform

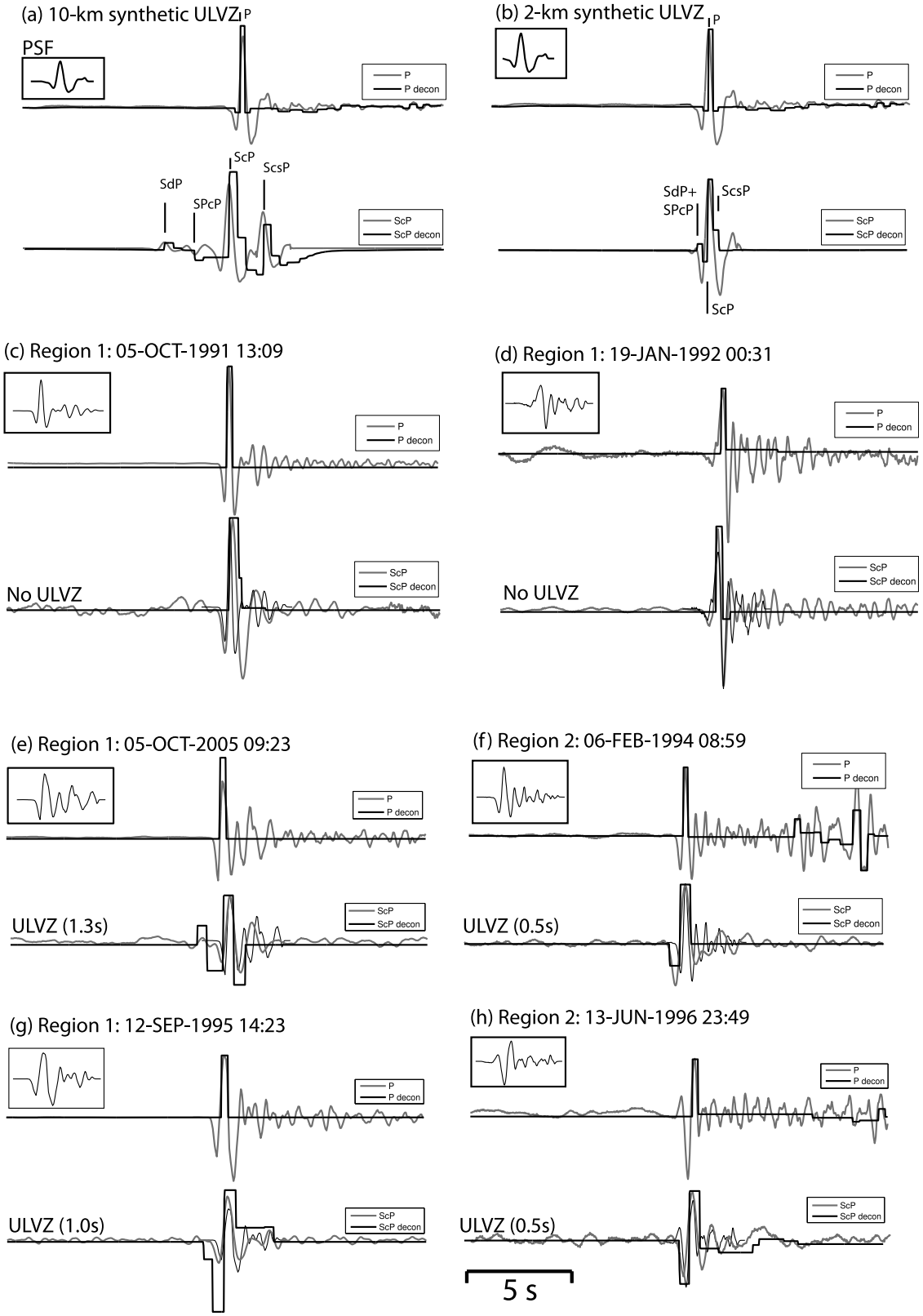
(a) 10-km synthetic ULVZ
PSF
P
P decon
ScP
ScsP
SdP
SPcP
ScP
ScP decon
(b) 2-km synthetic ULVZ
P
P decon
SdP+
SPcP
ScsP
ScP
ScP
ScP decon
(c) Region 1: 05-OCT-1991 13:09
P
P decon
ScP
ScP decon
No ULVZ
(d) Region 1: 19-JAN-1992 00:31
P
P decon
ScP
ScP decon
No ULVZ
(e) Region 1: 05-OCT-2005 09:23
P
P decon
ScP
ScP decon
ULVZ (1.3s)
(f) Region 2: 06-FEB-1994 08:59
P
P decon
ScP
ScP decon
ULVZ (0.5s)
(g) Region 1: 12-SEP-1995 14:23
P
P decon
ScP
ScP decon
ULVZ (1.0s)
(h) Region 2: 13-JUN-1996 23:49
P
P decon
ScP
ScP decon
ULVZ (0.5s)
5 s

Figure 5

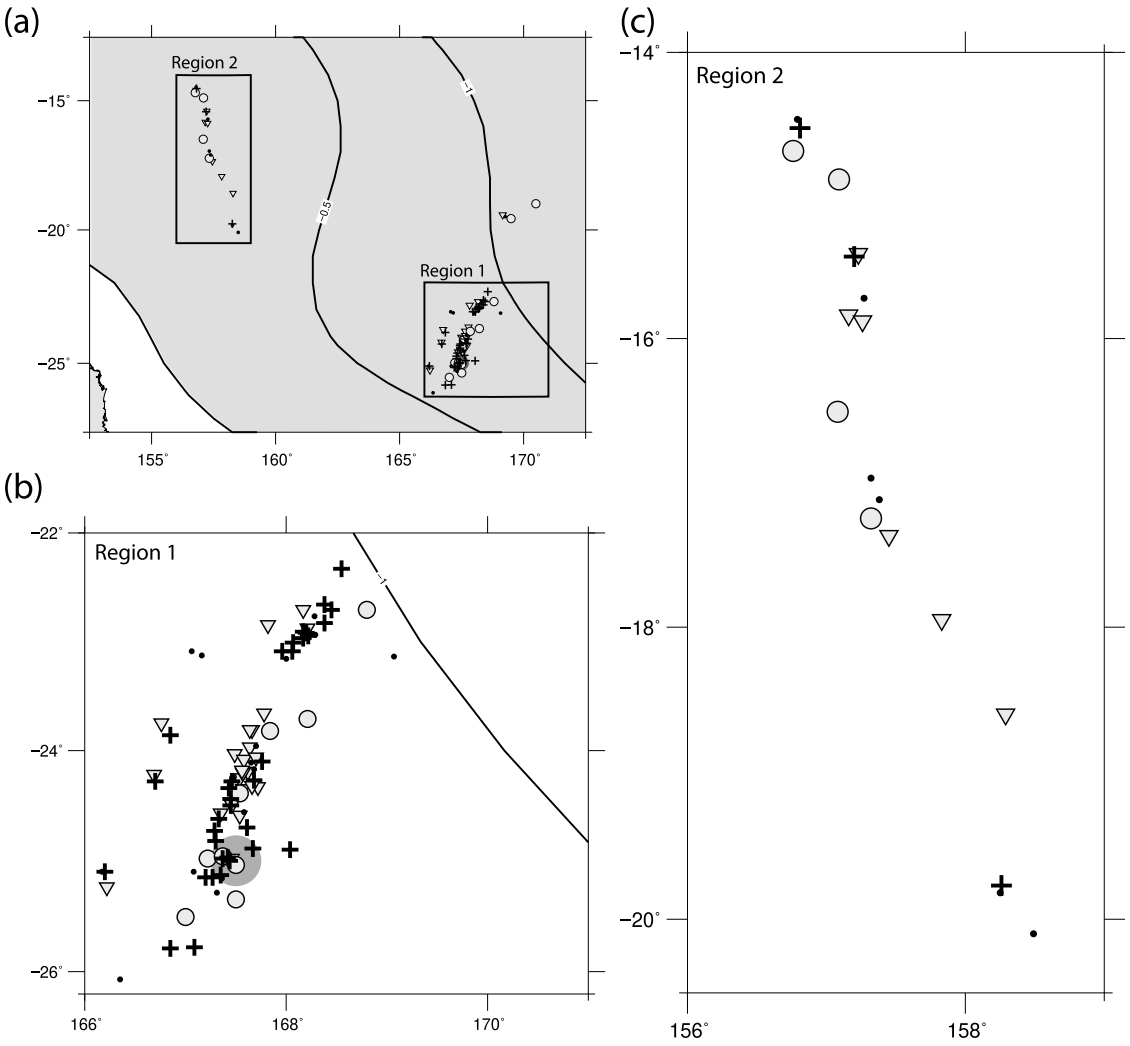

Figure 6. (a) Map of potential ULVZ detections from TV deconvolved *ScP* precursors. *ScP* waveforms are classified in three groups: (1) no *ScP* precursor in deconvolution (crosses), (2) *ScP* precursors with less than 1 s differential traveltime (inverted triangle), and (3) *ScP* precursors with more than 1 s differential traveltimes (circles). Furthermore, inconclusive results (mostly due to complicated *P* wavelets) are marked as black dots at the *ScP* reflection point. Contours give *S* wave velocity changes from tomography [*Ritsema and van Heijst*, 2002]. (b) Zoom into region 1. Symbols are the same as in Figure 6a. (c) Zoom into region 2. Symbols are the same as in Figure 6a.

Figure 5. Waveform examples of TV deconvolved *ScP* waveforms. Amplitudes are normalized to maximum peak-to-peak amplitudes except for the *P* waveform deconvolution normalized to zero-to-peak maximum amplitude. (a) Synthetic *ScP* waveform for a 10 km thick ULVZ (with *P* wave and *S* wave reductions of 10% and 30%, respectively, and 10% density increase). *ScP* precursors (*SdP*, *SPcP*) and postcursor (*ScSP*) are modeled in addition to the main CMB reflection (*ScP*). Top trace shows the synthetic *P* wavelet (gray line) and the deconvolution (black line) using the original *P* wavelet as point spread function (PSF) which is shown in the insert. Bottom trace shows the synthetic *ScP* waveform (gray line) and the deconvolution (black line) with marked arrivals. The timescale for all traces is given at the bottom of Figure 5. (b) Same as Figure 5a except with a thin ULVZ of 2 km thickness. A distinct precursor indicates the arrivals of the ULVZ generated phases. (c) Same as Figure 5a except no ULVZ precursor can be identified in the deconvolved *ScP* waveform. (d) Same as Figure 5c except no *ScP* precursor can be identified. (e) Same as Figure 5c sampling of region 1 except a strong precursor precedes *ScP* by about 1.3 s. (f) Same as Figure 5c except a ~0.5 s precursor can be identified. (g) Same as Figure 5c sampling of region 1 except a ~1.0 s can be identified. (h) Same as Figure 5c sampling of region 2 except a ~0.5 s precursor can be identified.

variations detectable after deconvolution (crosses in Figure 6), (2) precursors with differential traveltimes to *ScP* less than 1 s (inverted triangles in Figure 6), and (3) precursors with differential traveltimes to *ScP* more than 1 s (circles in Figure 6). Furthermore, several events yield inconclusive results mainly because of complicated *P* waveforms that produce complicated *ScP* deconvolved waveforms. These are marked with dots in Figure 6.

[26] Many of the events, especially in region 2, show precursors less than 1 s in front of *ScP* with many showing ~0.5 s lead time to *ScP*. This would correspond to a thin ULVZ with a thickness of 2–3 km assuming 10% and 30% V_P and V_S reductions, respectively. There is evidence for a 5–6 km thick ULVZ to the north of the "thick" ULVZ region identified by *Rost et al.* [2005, 2006] (Figure 6b). Nonetheless, the results do show quite some variability, and no coherent ULVZ structure can be identified from these results. This likely indicates ULVZ structure that changes on short scale lengths compared to the wavelengths of the 1 Hz data used here (~10 km).

[27] We note that some of the *ScP* precursors seem to be too big in amplitude to be explained by sensible ULVZ models, and we do not attempt to use the precursor information beyond a ULVZ detection. Any deconvolution introduces spurious energy in the deconvolved trace if there is any error (or spurious energy) in the representative empirical waveshape that is deconvolved from the other records. If the waveform structure in the *P* wave that is used for the *ScP* deconvolution is not representative of the impulse function or input shape to the *ScP* wave, the applied deconvolution will, as for any other deconvolution method, create artifact energy. Here we use a large enough data set to emphasize geographical patterns in the *ScP* waveforms.

[28] Region 1 consistently shows precursors with differential traveltimes to *ScP* larger than 1 s along the stretch of the north–south profile. But these precursor detections are interspersed with precursor nondetections. *ScP* precursors preceding *ScP* by less than 1 s seem to mainly exist toward the western and eastern edge of the profile. We note that few (only two detections are obvious) *ScP* precursors preceding *ScP* by more than 1 s are identified to the south of the thick ULVZ region (indicated by the gray circle in Figure 6b). The relatively thicker ULVZ of *Rost et al.* [2005] might therefore indicate just the thickest part of a broader ULVZ whose flanks are not detectable using standard *ScP* waveform variations since it is too thin (~5 km) to produce significant waveform variations in the nondeconvolved data outside of the area described by *Rost et al.* [2005]. The 5 km thin ULVZ might be surrounded by a halo of 2–3 km thick ULVZ, but the sparseness of the data and the many non-ULVZ detections preclude any conclusive answer to this.

[29] Region 2 is sampled by much less because of the lower *ScP* SNR in this data set and fewer events to start with. There is evidence for two groups (containing three events each) that sample thicker ULVZ with a thickness of ~6 km by showing *ScP* precursors leading *ScP* by ~1.5 s. These are separated by possibly thinner ULVZ (3 km) as detected by *ScP* precursors leading *ScP* by ~0.7 s. Nonetheless, the constraints on structures in this region are hindered by only 19 high-quality *ScP* recordings sampling the CMB in this area.

[30] To test the possibility that the variations in *ScP* waveforms do not originate from the interaction with a ULVZ at the reflection point, the correlation to event parameters has been tested. The events used span a large depth range from 365 to 631 km for region 1 and from 115 to 255 km for region 2. The precursor detection events have source depths of 410–631 km for region 1 and 120–255 km for region 2. The pattern of ULVZ detection, inconclusive results, and nondetections as shown in Figure 6 mirrors the exact source location since the same array (WRA) has been used for all events. We therefore conclude that the source location does not influence the *ScP* precursor detections. Because of the small magnitude of many events in the data set and the lack of available focal mechanism solutions, we did not test any possible correlation for this source parameter.

[31] Synthetic tests show that the increased sensitivity of *ScP* to ULVZ structure using TV deconvolved data pushes the vertical resolution limit of ULVZ thicknesses down to 2–3 km. In past work the *ScP* resolution threshold for ULVZ is normally stated to be around 5 km [*Rost and Revenaugh*, 2003; *Idehara et al.*, 2007], but this might be optimistic in light of the recent results, and we put the resolution of the array *ScP* waveform studies more toward 7 km (i.e., maximum separation time of *ScP* and the precursors time of ~1.7 s). Therefore, the TV deconvolution employed here leads to an important increase in resolution capabilities for ULVZ structure. Nonetheless, despite the increase of vertical resolution, data that are well explained by an absence of ULVZ structure could still contain an even thinner ULVZ, i.e., thinner than the 2–3 km resolution threshold; alternatively, a slightly thicker ULVZ (e.g., 5 km) with weaker velocity reductions than used in our synthetic modeling may go undetected. However, the latter case puts into question what should and should not be classified as "ultra" in ULVZ work.

[32] The area sampled here can also be sampled using the Alice Springs Array which is located a few hundred kilometers south of WRA. ASAR data have been used previously to resolve fine-scale internal ULVZ structure [*Rost et al.*, 2006]. Unfortunately, the ASAR data do not give stable results in the TV deconvolution because of noise conditions.

[33] The current results indicate that ULVZ structure in this region might be highly complicated and might change on very short scale lengths. In case of such a scenario we expect strong waveform variations due to waveform effects such as focusing and de-focusing as well as multipathing in the 3-D structure. These effects are not fully captured by most modeling attempts of *ScP* waveforms that in general assume 1-D layering only. Higher-resolution full 3-D wavefield propagation simulations (at high frequency) are needed to understand these effects better.

[34] Our study region is located at the boundary of a large low shear velocity province (LLSVP) imaged by global tomography beneath the central Pacific [*Masters et al.*, 1996; *Mégnin and Romanowicz*, 2000; *Ritsema and van Heijst*, 2000; *Grand*, 2002; *Antolik et al.*, 2003]. This region is indicated in gray in Figure 6a, and we define the 0% velocity change boundary as the boundary of the LLSVP. *He et al.* [2006] located a possible edge of the LLSVP that almost coincides with the location of the 0% velocity change boundary in this region (Figure 1c). While the *ScP* reflection points in region 1 are located in an area

where tomographic images detect *S* wave velocity reductions of 0.5%–1.0% relative to PREM, region 2 samples an area with smaller *S* wave velocity reductions of only 0%–0.5% in this model. The edge of the LLSVP is not well defined, and both regions might lie within the LLSVP but nonetheless close to the LLSVP margin.

[35] If partially molten material is the source for the seismic velocity reduction within ULVZs, ULVZs should exist everywhere where the temperature of the mantle rock crosses the solidus for the appropriate chemistry [*Garnero and McNamara*, 2008]. Hotter regions of the mantle should then show the thickest ULVZ due to the higher melt production. With region 1 showing evidence for an easily detected ULVZ of 8.5 km thickness and evidence for 5–6 km thick ULVZ around it, this region might be hotter than region 2 which shows evidence only for thinner ULVZ structure. Because of the lack of *ScP* reflection points outside of the LLSVP, it is difficult to estimate the extent of ULVZ outside of the 0% velocity change isoline, but SP_dKS data indicate the absence of ULVZ toward that direction [*Thorne and Garnero*, 2004].

[36] Geodynamic modeling shows that LLSVP might be chemically distinct features of the lower mantle [*McNamara and Zhong*, 2005; *Tan and Gurnis*, 2005, 2007]. The large low-velocity regions dominant in tomographic images of the lower mantle beneath the Pacific and Africa have been found to likely be of thermochemical origin [*Wen*, 2001; *McNamara and Zhong*, 2005] rather than purely thermal features. Geodynamic modeling [*McNamara and Zhong*, 2005] shows that dense thermochemical piles (DTCP) can account for the low seismic velocities in these areas. The geodynamical modeling also shows that DTCPs are hotter than the surrounding mantle and are internally convecting (with conduction being the dominant heat transfer mechanism across the boundary of the DTCP). The hottest regions of the DTCP can be found below upwellings within the DTCP, such as along the DTCP margins [*Rost et al.*, 2005; *Garnero and McNamara*, 2008] and in areas of stagnant flow at the edges of the piles [*McNamara and Zhong*, 2005]. Indeed, several seismic studies find evidence for ULVZs at the edges of the DTCP [*Rost et al.*, 2005, 2006; *Lay et al.*, 2006], but this conclusion is hindered by the lack of geographical sampling in high-resolution ULVZ analyses. Further evidence for the possibility that ULVZs are likely formed at the edges of DTCP comes from geodynamical modeling including a dense basal layer in addition to denser material within the DTCP and normal density mantle (A. McNamara et al., Tracking deep mantle reservoirs with ultralow velocity zones, submitted to *Earth and Planetary Science Letters*, 2010). These simulations show that the edges of the DTCP and upwellings within the DTCP are associated with the thickest aggregation of the densest material (i.e., ULVZ material). The amount of this aggregation is strongly dependent on the viscosity of the dense material, but the modeling shows that the topography of thick regions of dense material can be dynamically supported by the convection within the DTCP. Interestingly, the geodynamic modeling shows that because of different viscous coupling, the ULVZ should be asymmetric with the thinner parts toward the LLSVP (A. McNamara et al., submitted manuscript, 2009). This asymmetry is similar to the ULVZ behavior observed here although the interpretation is hindered by the limited lateral sampling in this study and the ill-defined boundary of the LLSVP.

[37] The results presented here indicate that thin ULVZ might be present below the seismic resolution level in wide areas of the CMB and that previous ULVZ detections are biased toward detecting thick ULVZ regions only. This might indicate a dynamical origin of ULVZ that might be related to partially molten or chemically distinct material that is deposited in areas of stagnant mantle flow, e.g., at the edges of LLSVP or beneath upwellings.

5. Conclusion

[38] For a better understanding of the origin, evolution, and dynamics of ULVZs a better characterization of ULVZ regions versus non-ULVZ regions is necessary. Unfortunately, even regions that can be characterized as non-ULVZ regions by seismic methods can actually contain ULVZ below the seismic resolution (i.e., too weak or too thin) to be detected by current seismic waveform methods. Here we present the application of a TV deconvolution method that allows us to collect evidence for ultrathin ULVZ in regions that were previously characterized as non-ULVZ regions. The deconvolved *ScP* waveforms for a region east of Australia show evidence for thin ULVZs with thicknesses of 2–3 km only. A region bordering the northern edge of a previously detected 8.5 km thick ULVZ area was imaged as having a ULVZ with 5–6 km thickness.

[39] The two studied regions sample the edge of a large low shear velocity structure beneath the Pacific with the eastern region (region 1) sampling lower *S* wave velocities in the range of 0.5%–1% lower [*Ritsema and van Heijst*, 2002] than PREM [*Dziewonski and Anderson*, 1981]. Region 2, to the west of region 1, samples deep mantle having milder *S* wave velocity reductions from 0% to 0.5% and has been imaged with extremely thin ULVZ. The TV deconvolution method enables us to detect much thinner ULVZ structure; the *ScP* probe ULVZ detection threshold has been reduced from 5–7 km to about 2–3 km, assuming V_P and V_S reductions of 10% and 30%, respectively, and 10% density increase.

[40] These results support the hypothesis that ULVZs might preferentially exist at the margins of tomographically imaged large low shear velocity provinces that might be chemically distinct. Applying the TV deconvolution to higher-frequency array data might further decrease the minimum detectable ULVZ thickness. Geodynamical modeling shows that dense ULVZ material can be dynamically supported at the margins of DTCP and can create topography comparable to that seismically observed (A. McNamara et al., submitted manuscript, 2009). The results presented here show evidence that previously detected areas of 8.5 km thick ULVZ at the margins of the Pacific LLSVP are surrounded by thinner ULVZ, which is in good agreement with dynamical modeling.

[41] **Acknowledgments.** We thank S. Grand for the Futterman t^* code used for the differential t^* analysis. We also thank the AWE Blacknest data center for providing access to the WRA data. Data analysis was performed using Seismic Handler [*Stammler*, 1993]. Maps were produced using GMT [*Wessel and Smith*, 1998]. We thank the Associate Editor Stephane Rondenay and an anonymous reviewer for comments that

improved this manuscript. E.J.G. was partially supported by U.S. National Science Foundation grants EAR-0453944 and EAR-0711401.

References

Antolik, M., Y. Gu, G. Ekstrom, and A. Dziewonski (2003), J362D28: A new joint model of compressional and shear velocity in the Earth's mantle, *Geophys. J. Int.*, *153*(2), 443–466, doi:10.1046/j.1365-246X.2003.01910.x.

Avants, M., T. Lay, and E. Garnero (2006a), A new probe of ULVZ *S* wave velocity structure: Array stacking of *ScS* waveforms, *Geophys. Res. Lett.*, *33*, L07314, doi:10.1029/2005GL024989.

Avants, M., T. Lay, S. Russell, and E. Garnero (2006b), Shear velocity variation within the D″ region beneath the central Pacific, *J. Geophys. Res.*, *111*, B05305, doi:10.1029/2004JB003270.

Bataille, K., and F. Lund (1996), Strong scattering of short-period seismic waves by the core-mantle boundary and the *P*-diffracted wave, *Geophys. Res. Lett.*, *23*(18), 2413–2416, doi:10.1029/96GL02225.

Berryman, J. (2000), Seismic velocity decrement ratios for regions of partial melt in the lower mantle, *Geophys. Res. Lett.*, *27*(3), 421–424, doi:10.1029/1999GL008402.

Bock, G., and J. Clements (1982), Attenuation of short-period P, *PcP*, *ScP*, and PP waves in the Earth's mantle, *J. Geophys. Res.*, *87*(B5), 3905–3918, doi:10.1029/JB087iB05p03905.

Buffett, B., E. Garnero, and R. Jeanloz (2000), Sediments at the top of Earth's core, *Science 290*(5495), 1338–1342, doi:10.1126/science.290.5495.1338.

Bullen, K. (1949), An Earth model based on a compressibility-pressure hypothesis, *Mon. Not. R. Astron. Soc.*, *109*(6), 50–59.

Capon, J. (1969), High-resolution frequency-wave number spectrum analysis, *Proc. IEEE*, *57*(8), 1408–1418, doi:10.1109/PROC.1969.7278.

Carpenter, E., and E. Flinn (1965), Attenuation of teleseismic body waves, *Nature*, *207*(4998), 745–746, doi:10.1038/207745b0.

Castle, J., and R. van der Hilst (2000), The core-mantle boundary under the Gulf of Alaska: No ULVZ for shear waves, *Earth Planet. Sci. Lett.*, *176*(3–4), 311–321, doi:10.1016/S0012-821X(00)00027-3.

Cerveny, V. (1985), Gaussian beam synthetic seismograms, *J. Geophys.*, *58*(1–3), 44–72.

Cleary, J., C. Wright, and K. Muirhead (1968), The effects of local structure upon measurements of the travel time gradient at the Warramunga seismic array, *Geophys. J. R. Astron. Soc.*, *16*(1), 21–29.

Cormier, V. (1999), Anisotropy of heterogeneity scale lengths in the lower mantle from PKIKP precursors, *Geophys. J. Int.*, *136*(2), 373–384, doi:10.1046/j.1365-246X.1999.00736.x.

Davis, J., and I. Henson (1993), User's guide to Xgbm: An X-Windows system to compute Gaussian beam synthetic seismograms, contract F29601-91-C-DBO4, Teledyne Geotech Alexandria Lab., Alexandria, Va.

Dobson, D., and J. P. Brodholt (2005), Subducted banded iron formations as a source of ultralow-velocity zones at the core-mantle boundary, *Nature*, *434*(7031), 371–374, doi:10.1038/nature03430.

Dziewonski, A., and D. Anderson (1981), Preliminary reference Earth model, *Phys. Earth Planet. Inter.*,*25*(4), 297–356, doi:10.1016/0031-9201(81)90046-7.

Earle, P., and P. Shearer (1998), Observations of high-frequency scattered energy associated with the core phase *PKKP*, *Geophys. Res. Lett.*, *25*(3), 405–408, doi:10.1029/97GL53365.

Garnero, E. (2000), Heterogeneity of the lowermost mantle, *Annu. Rev. Earth Planet. Sci.*, *28*, 509–537, doi: 10.1146/annurev.earth.28.1.509.

Garnero, E., and D. Helmberger (1995), A very slow basal layer underlying large-scale low-velocity anomalies in the lower mantle beneath the Pacific: Evidence from core phases, *Phys. Earth Planet. Inter.*, *91*(1–3), 161–176, doi:10.1016/0031-9201(95)03039-Y.

Garnero, E., and D. Helmberger (1998), Further structural constraints and uncertainties of a thin laterally varying ultralow-velocity layer at the base of the mantle, *J. Geophys. Res.*, *103*(B6), 12,495–12,509, doi: 10.1029/98JB00700.

Garnero, E., and R. Jeanloz (2000), Fuzzy patches on the Earth's core-mantle boundary?, *Geophys. Res. Lett.*, *27*(17), 2777–2780, doi:10.1029/2000GL008498.

Garnero, E., and A. McNamara (2008), Structure and dynamics of Earth's lower mantle, *Science, 320*(5876), 626–628, doi:10.1126/science.1148028.

Garnero, E., and J. Vidale (1999), *ScP*; A probe of ultralow velocity zones at the base of the mantle, *Geophys. Res. Lett.*, *26*(3), 377–380, doi:10.1029/1998GL900319.

Garnero, E., J. Revenaugh, Q. Williams, T. Lay, and L. Kellogg (1998), Ultralow velocity zone at the core-mantle boundary, in *The Core-Mantle Boundary Region*, *Geodyn. Ser.*, vol. *28*, edited by M. Gurnis et al., pp. 319–334, AGU, Washington, D. C.

Garnero, E., V. Maupin, T. Lay, and M. Fouch (2004), Variable azimuthal anisotropy in Earth's lowermost mantle, *Science*, *306*(5694), 259–261, doi:10.1126/science.1103411.

Garnero, E., A. McNamara, M. Thorne, and S. Rost (2007), Fine-scale ultra-low velocity zone layering at the core-mantle boundary and superplumes, in *Superplumes: Beyond Plate Tectonics*, edited by D. A. Yuen et al., pp. 139–158, Springer, New York, doi:10.1007/978-1-4020-5750-2_6.

Grand, S. (2002), Mantle shear-wave tomography and the fate of subducted slabs, *Philos. Trans. R. Soc. London A*, *360*(1800), 2475–2491.

He, Y., L. Wen, and T. Zheng (2006), Geographic boundary and shear wave velocity structure of the "Pacific anomaly" near the core-mantle boundary beneath western Pacific, *Earth Planet. Sci. Lett.*, *244*(1–2), 302–314, doi:10.1016/j.epsl.2006.02.007.

Hedlin, M., and P. Shearer (2000), An analysis of large-scale variations in small-scale mantle heterogeneity using Global Seismographic Network recordings of precursors to PKP, *J. Geophys. Res.*, *105*(B6), 13,655–13,673, doi:10.1029/2000JB900019.

Helffrich, G., and S. Kaneshima (2004), Seismological constraints on core composition from Fe-O-S liquid immiscibility, *Science*, *306*(5705), 2239–2242, doi:10.1126/science.1101109.

Hutko, A., T. Lay, J. Revenaugh, and E. Garnero (2008), Anticorrelated seismic velocity anomalies from post-perovskite in the lowermost mantle, *Science*, *320*(5879), 1070–1074, doi:10.1126/science.1155822.

Idehara, K., A. Yamada, and D. Zhao (2007), Seismological constraints on the ultralow velocity zones in the lowermost mantle from core-reflected waves, *Phys. Earth Planet. Inter.*, *165*(1–2), 25–46, doi:10.1016/j.pepi.2007.07.005.

Kendall, J., and P. Silver (1996), Constraints from seismic anisotropy on the nature of the lowermost mantle, *Nature*, *381*(6581), 409–412, doi:10.1038/381409a0.

Kito, T., S. Rost, C. Thomas, and E. Garnero (2007), New insights into the *P* and *S* wave velocity structure of the D″ discontinuity beneath the Cocos Plate, *Geophys. J. Int.*, *169*(2), 631–645, doi:10.1111/j.1365-246X.2007.03350.x.

Labrosse, S., J. Hernlund, and N. Coltice (2007), A crystallizing dense magma ocean at the base of the Earth's mantle, *Nature*, *450*(7171), 866–869, doi:10.1038/nature06355.

Lay, T., and D. Helmberger (1983), A lower mantle *S* wave triplication and the shear velocity structure of D″, *Geophys. J. R. Astron. Soc.*, *75*, 799–837.

Lay, T., Q. Williams, E. Garnero, L. Kellogg, and M. Wysession (1998), Seismic wave anisotropy in the D″ region and its implications, in *The Core-Mantle Boundary Region*, *Geodyn. Ser.*, vol.*28*, edited by M. Gurnis et al., 299–318, AGU, Washington, D. C.

Lay, T., E. Garnero, and Q. William (2004), Partial melting in a thermo-chemical boundary layer at the base of the mantle, *Phys. Earth Planet. Inter.*, *146*(3–4), 441–467, doi:10.1016/j.pepi.2004.04.004.

Lay, T., J. Hernlund, E. Garnero, and M. Thorne (2006), A post-perovskite lens and D″ heat flux beneath the central Pacific, *Science*, *314*(5803), 1272–1276, doi:10.1126/science.1133280.

Mao, W., H. Mao, W. Sturhahn, J. Zhao, V. Prakapenka, Y. Meng, J. Shu, Y. Fei, and R. Hemley (2006), Iron-rich post-perovskite and the origin of ultralow-velocity zones, *Science*, *312*(5773), 564–565, doi:10.1126/science.1123442.

Masters, G., S. Johnson, G. Laske, H. Bolton, and J. H. Davies (1996), A shear-velocity model of the mantle, *Philos. Trans. R. Soc. London A*, *354*(1711), 1385–1410.

McNamara, A., and S. Zhong (2005), Thermochemical structures beneath Africa and the Pacific Ocean, *Nature*, *437*(7062), 1136–1139, doi:10.1038/nature04066.

Mégnin, C., and B. Romanowicz (2000), The three-dimensional shear velocity structure of the mantle from the inversion of body, surface and higher-mode waveforms, *Geophys. J. Int.*, *143*(3), 709–728, doi:10.1046/j.1365-246X.2000.00298.x.

Mori, J., and D. Helmberger (1995), Localized boundary-layer below the mid-Pacific velocity anomaly identified from a *PcP* precursor, *J. Geophys. Res.*, *100*(B10), 20,359–20,365, doi:10.1029/95JB02243.

Nakagawa, T., and P. Tackley (2004), Thermo-chemical structure in the mantle arising from a three-component convective system and implications for geochemistry, *Phys. Earth Planet. Inter.*, *146*(1–2), 125–138, doi:10.1016/j.pepi.2003.05.006.

Persh, S., J. Vidale, and P. Earle (2001), Absence of short-period ULVZ precursors to *PcP* and *ScP* from two regions of the CMB, *Geophys. Res. Lett.*, *28*(2), 387–390, doi:10.1029/2000GL011607.

Reasoner, C., and J. Revenaugh (2000), *ScP* constraints on ultralow-velocity zone density and gradient thickness beneath the Pacific, *J. Geophys. Res.*, *105*(B12), 28,173–28,182, doi:10.1029/2000JB900331.

Revenaugh, J., and R. Meyer (1997), Seismic evidence of partial melt within a possibly ubiquitous low-velocity layer at the base of the mantle, *Science*, *277*(5326), 670–673, doi:10.1126/science.277.5326.670.

Ritsema, J., and H. van Heijst (2000), New seismic model of the upper mantle beneath Africa, *Geology*, *28*(1), 63–66, doi:10.1130/0091-7613(2000)28<63:NSMOTU>2.0.CO;2.

Ritsema, J., and H. van Heijst (2002), Constraints on the correlation of *P* and *S* wave velocity heterogeneity in the mantle from P, PP, PPP and PKPab traveltimes, *Geophys. J. Int.*, *149*(2), 482–489, doi:10.1046/j.1365-246X.2002.01631.x.

Rokosky, J., T. Lay, and E. Garnero (2006), Small-scale lateral variations in azimuthally anisotropic D″ structure beneath the Cocos Plate, *Earth Planet. Sci. Lett.*, *248*(1–2), 411–425, doi:10.1016/j.epsl.2006.06.005.

Rondenay, S., and K. Fischer (2003), Constraints on localized core-mantle boundary structure from multichannel, broadband SKS coda analysis, *J. Geophys. Res.*, *108*(B11), 2537, doi:10.1029/2003JB002518.

Rost, S., and J. Revenaugh (2001), Seismic detection of rigid zones at the top of the core, *Science*, *294*(5548), 1911–1914, doi:10.1126/science.1065617.

Rost, S., and J. Revenaugh (2003), Small-scale ultralow-velocity zone structure imaged by *ScP*, *J. Geophys. Res.*, *108*(B1), 2056, doi:10.1029/2001JB001627.

Rost, S., and C. Thomas (2002), Array seismology: Methods and applications, *Rev. Geophys.*, *40*(3), 1008, doi:10.1029/2000RG000100.

Rost, S., E. Garnero, Q. Williams, and M. Manga (2005), Seismological constraints on a possible plume root at the core-mantle boundary, *Nature*, *435*(7042), 666–669, doi:10.1038/nature03620.

Rost, S., E. Garnero, and Q. Williams (2006), Fine-scale ultralow-velocity zone structure from high-frequency seismic array data, *J. Geophys. Res.*, *111*, B09310, doi:10.1029/2005JB004088.

Rost, S., E. Garnero, M. Thorne, and A. Hutko (2010), On the absence of an ultra-low velocity zone in the North Pacific, *J. Geophys. Res.*, *115*, B04312, doi:10.1029/2009JB006420.

Stammler, K. (1993), Seismichandler-Programmable multichannel data handler for interactive and automatic processing of seismological analyses, *Comput. Geosci.*, *19*(2), 135–140, doi:10.1016/0098-3004(93)90110-Q.

Stefan, W., E. Garnero, and R. Renaut (2006), Signal restoration through deconvolution applied to deep mantle seismic probes, *Geophys. J. Int.*, *167*(3), 1353–1362, doi:10.1111/j.1365-246X.2006.03124.x.

Tan, E., and M. Gurnis (2005), Metastable superplumes and mantle compressibility, *Geophys. Res. Lett.*, *32*, L20307, doi:10.1029/2005GL024190.

Tan, E., and M. Gurnis (2007), Compressible thermochemical convection and application to lower mantle structures, *J. Geophys. Res.*, *112*, B06304, doi:10.1029/2006JB004505.

Thomas, C., E. Garnero, and T. Lay (2004), High-resolution imaging of lowermost mantle structure under the Cocos plate, *J. Geophys. Res.*, *109*, B08307, doi:10.1029/2004JB003013.

Thomas, C., J. Kendall, and G. Helffrich (2009), Probing two low-velocity regions with PKP b-caustic amplitudes and scattering, *Geophys. J. Int.*, *178*(1), 503–512, doi:10.1111/j.1365-246X.2009.04189.x.

Thorne, M., and E. Garnero (2004), Inferences on ultralow-velocity zone structure from a global analysis of *SPdKS* waves, *J. Geophys. Res.*, *109*, B08301, doi:10.1029/2004JB003010.

Tolstikhin, I., and A. Hofmann (2005), Early crust on top of the Earth's core, Phys. *Earth Planet. Inter.*, *148*(2–4), 109–130, doi:10.1016/j.pepi.2004.05.011.

van der Hilst, R., M. de Hoop, P. Wang, S. Shim, P. Ma, and L. Tenorio (2007), Seismostratigraphy and thermal structure of Earth's core-mantle boundary region, *Science 315*(5820), 1813–1817, doi:10.1126/science.1137867.

Vidale, J., and H. Benz (1992), A sharp and flat section of the core mantle boundary, *Nature*, *359*(6396), 627–629, doi:10.1038/359627a0.

Vidale, J., and H. Benz (1993), Sesimological mapping of fine structure near the base of the Earth's mantle, *Nature*, *361*(6412), 529–532, doi:10.1038/361529a0.

Vidale, J., and M. Hedlin (1998), Evidence for partial melt at the core-mantle boundary north of Tonga from the strong scattering of seismic waves, *Nature*, *391*(6668), 682–685, doi:10.1038/35601.

Vogel, C. R. (2002), *Computational Methods for Inverse Problems*, 1st ed., Soc. for Ind. and Appl. Math, Philadelphia, Pa.

Weber, M. (1988), Computation of body-wave seismograms in absorbing 2-D media using the Gaussian beam method: Comparison with exact methods, *Geophys. J.*, *92*(1), 9–24, doi:10.1111/j.1365-246X.1988.tb01116.x.

Wen, L. (2000), Intense seismic scattering near the Earth's core-mantle boundary beneath the Comoros hotspot, *Geophys. Res. Lett.*, *27*(22), 3627–3630, doi:10.1029/2000GL011831.

Wen, L. (2001), Seismic evidence for a rapidly varying compositional anomaly at the base of the Earth's mantle beneath the Indian Ocean, *Earth Planet. Sci. Lett.*, *194*(1–2), 83–95, doi:10.1016/S0012-821X(01)00550-7.

Wen, L., and D. Helmberger (1998), Ultra-low velocity zones near the core-mantle boundary from broadband PKP precursors, *Science*, *279*(5357), 1701–1703, doi:10.1126/science.279.5357.1701.

Wessel, P., and W. Smith (1998), New, improved version of the Generic Mapping Tools, *Eos Trans. AGU*, *79*, 579.

Williams, Q., and E. Garnero (1996), Seismic evidence for partial melt at the base of Earth's mantle, *Science*, *273*(5281), 1528–1530, doi:10.1126/science.273.5281.1528.

Wookey, J., and J. Kendall (2008), Constraints on lowermost mantle mineralogy and fabric beneath Siberia from seismic anisotropy, *Earth Planet. Sci. Lett.*, *275*(1–2), 32–42, doi:10.1016/j.epsl.2008.07.049.

E. J. Garnero, School of Earth and Space Exploration, Arizona State University, PO Box 871404, Tempe, AZ 85287, USA.

S. Rost, Institute of Geophysics and Tectonics, School of Earth and Environment, University of Leeds, 15-19 Hyde Ter., Leeds LS2 9JT, UK. (s.rost@leeds.ac.uk)

W. Stefan, Department of Computational and Applied Mathematics, Rice University, 6100 Main St., MS 134, Houston, TX 77005, USA.